

Deciphering Grain Boundary Properties in High-Entropy Alloys in a 5D Space: Coupled Segregation and Disordering

Chongze Hu^{1,2}, Jian Luo^{1,2*}

1. Program of Materials Science and Engineering, University of California San Diego, La Jolla, California 92093, USA

2. Department of Nanoengineering, University of California San Diego, La Jolla, California 92093, USA

*Corresponding author. E-mail: jluo@alum.mit.edu

Abstract

Like any other conventional alloys, grain boundaries (GBs) can influence the microstructural evolution and properties of high-entropy alloys (HEAs). However, a fundamental understanding of GBs in HEAs is lacking because of the complex couplings of GB segregation and disorder, which can also produce new phenomena and challenge the classical GB segregation models. Here, by combining hybrid Monte Carlo and molecular dynamics simulations and artificial neural networks, we demonstrate the feasibility of predicting the GB properties as functions of four independent compositional degrees of freedoms and temperature in a five-dimensional (5D) space. Furthermore, unique GB segregation behaviors are revealed; for example, the site competition in more ordered GBs leads to weak segregation in medium-entropy alloys, while the segregation of multiple elements coupled with GB disordering can induce strong co-segregation in HEAs. In general, we find that GB disorder can significantly influence segregation, which are not considered in the classical models. A surrogate data-based analytical model is proposed, which predicts that GB segregation minimizes at a compensation temperature of ~1388 K in the Cantor alloy. This study not only provides a new paradigm enabling prediction of GB properties in a 5D space, but also reveal the new coupled segregation and disordering effects in HEAs.

Introduction

Since the Bronze and Steel Ages, the development of every major class of metallic alloys, such as the Cu, Fe, Al, Ti, and Ni-based alloys, have revolutionized technologies and changed our daily lives. High-entropy alloys (HEAs), also known as multi-principal element alloys (MPEAs) or complex concentrated alloys (CCA), represent the newest class of alloys that attract significant research interest¹⁻⁴. The vast composition space of HEAs offers immense opportunities for designing materials for various applications.

In every class of polycrystalline alloys, grain boundaries (GBs) exist ubiquitously^{5,6}. The elemental segregation (*a.k.a.* adsorption in the interfacial thermodynamics) at GBs is a critical phenomenon because it can change microstructural evolution⁷⁻⁹ and govern a broad range of materials properties¹⁰⁻¹². Even though the GB segregation have been extensively researched for decades, most prior studies and models are based on alloys with one primary (principal) element¹³⁻²⁰. Moreover, the effects of interfacial disordering on segregation is typically not considered in the classical site-occupying models¹³⁻¹⁵. The GB segregation in the emerging HEAs containing five or more principal elements are hitherto only investigated by few experimental^{21,22} and theoretical^{23,24} studies. The underlying mechanisms of GB segregation in HEAs are elusive and a predictive model does not exist, which motivate this study.

In a broader perspective, GBs can be considered as two-dimensional (2D) interfacial phases⁶, which are also named as “complexions”^{25,26} to differentiate them from thin precipitated layers of 3D bulk phases. Notably, GB diagrams, which represent GB states or properties as functions of thermodynamic variables such as temperature and bulk composition (representing chemical potentials), have been developed (as the GB counterparts to bulk phase diagrams, albeit the GB phase-like transitions can be first-order in some systems or continuous in other cases). To date, various GB diagrams have been constructed for binary and ternary systems^{19,20,25,27}, but they are rarely developed for multicomponent systems²⁸, certainly not for HEAs, owing to the increasing complexity. For example, the four independent compositional degrees of freedom (DOFs) of CrMnFeCoNi plus temperature make it difficult to map out GB properties in a 5D space by conventional methods. Furthermore, most prior studies of GBs focused on symmetric tilt or twist GBs that are relatively easy to image or model. The more general GBs (asymmetric GB with mixed twist and tilt features), which are ubiquitous in polycrystalline materials and often the weak links

chemically and mechanically^{27,29}, are still scarcely studied.

Herein, by combining the high-throughput hybrid Monte Carlo/molecular dynamic (MC/MD) simulations and artificial neural networks (ANN), we demonstrate the feasibility of predicting the GB properties as functions of four compositional DOFs and temperature in a 5D space for a representative general GB in $\text{Cr}_x\text{Mn}_y\text{Fe}_z\text{Co}_l\text{Ni}_m$ HEAs. Our MC/MD simulations also reveal the unrecognized importance of interfacial disorder in influencing GB segregation that can produce new phenomena in HEAs. Furthermore, a data-based analytical model (DBAM) is proposed to conveniently represent GB segregation and disordering in HEAs and reveal features that cannot be captured by classical models. Interestingly, this model predicts the almost (albeit not complete) vanishing of GB segregation/depletion of all elements almost simultaneously at a critical (compensation) temperature (~ 1388 K for the $\text{Cr}_x\text{Mn}_y\text{Fe}_z\text{Co}_l\text{Ni}_m$ HEAs).

Workflow of machine learning prediction and beyond

The workflow of ANN prediction for GB properties is displayed in Fig. 1. First, we selected a $\Sigma 81$ mixed GB to represent general GBs. We randomly generated 258 compositions out of 1371 possible choices by varying the amount of each element from 5% to 35% with a step of 5%. Second, principal components analysis (PCA) was used to ensure the 258 selected compositions are sufficiently randomly (Supplementary Discussion 1). Third, the high-throughput isothermal-isobaric (constant NPT) ensemble hybrid MC/MD simulations were carried out to calculate the adsorption amounts (*i.e.*, GB excesses of solutes: Γ_{Cr} , Γ_{Mn} , Γ_{Fe} , Γ_{Co} , Γ_{Ni}), GB excess of disorder (Γ_{Dis}), and GB free volume (V_{Free}), as well as bulk composition of each element (to map out a relation between bulk composition and chemical potential), from 1000 K to 1300 K with a temperature step of 100 K. Fourth, the MC/MD-simulated dataset was used to train, evaluate, and test ANN models to predict six GB properties (excluding V_{Free} due to a weak correlation to be discussed later). Here, the five bulk compositions and temperature are used as input parameters (Fig. 1d). Next, the well-trained ANN models are used to predict GB property diagrams with multiple variables. For example, we can generate isothermal sections of Γ_{Cr} for $\text{Cr}_x\text{Mn}_y\text{Fe}_z\text{Co}_{0.2}\text{Ni}_{0.2}$ subsystem, where $x + y + z = 0.6$, from 1000 to 1200 K (Fig. 1f). See Methods for further details.

It is worth noting that we first performed benchmark simulations to validate our NPT -based hybrid MC/MD method by comparing it with prior NVT -based MC simulations²⁴ as well as

experiments^{21,22,30}; see Supplementary Discussion 2.

In separate thrusts (in parallel with the ANN prediction), we analyzed MC/MD-simulated GB structures to decipher the couplings of GB segregation and disordering in HEAs and subsequently developed an analytical model to predict GB properties (Fig. 1f), which will be elaborated later.

ANN performance for predicting GB diagrams

The dataset generated by 1032 MC/MD simulations have been used to train, evaluate, and test one-layer single-task ANN models to predict six GB properties (Γ_{Cr} , Γ_{Mn} , Γ_{Fe} , Γ_{Co} , Γ_{Ni} , and Γ_{Dis}). The histogram of root-mean-square errors (RMSEs) was used to assess the ANN performance. Notably, the ANN models are fairly accurate to predict the values of Γ_{Co} , Γ_{Fe} , Γ_{Cr} , and Γ_{Mn} with small RMSEs (Supplementary Fig. S4). The accuracies are further supported by the parity plots between ANN predictions and MC/MD simulations, where the promising linear relations are achieved for Γ_{Cr} , Γ_{Mn} , Γ_{Fe} , and Γ_{Co} (see Fig. 2b and Supplementary Fig. S3). Relatively large deviations are found for Γ_{Ni} and Γ_{Dis} , which can be ascribed to the weak segregation of Ni and large uncertainty in quantifying Γ_{Dis} . Overall, the ANN models are robust to predict GB properties, especially for moderate and strong segregation (*e.g.*, Cr and Mn) and depletion elements (*e.g.*, Fe and Co) at HEA GBs.

To further validate our ANN models, we adopt an structural similarity index (SSIM; 1 = same and 0 = different) to compare the similarity of ANN-predicted binary GB diagrams *vs.* MC/MD simulations; representative GB diagrams are shown in Figs. 2b-c. The SSIM histogram (Supplementary Fig. S5) shows the high values (~0.88-0.89) for most Γ_{Cr} , Γ_{Mn} , Γ_{Fe} , and Γ_{Co} diagrams, but relatively low values (~0.63-0.66) for Γ_{Ni} and Γ_{Dis} diagrams. This is consistent with the prior analysis based on RMSEs. See further discussion in Supplementary Discussion 3.

Interestingly, ANN predictions can outperform MC/MD simulations in two aspects. First, ANN models can suppress the MC/MD errors caused by the large thermal noises at high temperatures (Supplementary Figs. S17-S22) by a smoothing effect. Second, the ANN models become more convenient than MC/MD simulations to predict GB diagrams with multiple variables. For example, Fig. 2d-i shows the ANN-predicted ternary GB adsorption and disorder diagrams in $\text{Cr}_x\text{Mn}_{0.2}\text{Fe}_y\text{Co}_{0.2}\text{Ni}_z$ (where $x + y + z = 0.6$) at 1000 K. More ANN-predicted GB diagrams can be found in Supplementary Figs. S17-S29.

Finally, the efficient ANN models make it possible to map out GB properties as functions of four independent compositional DOFs and temperature in a 5D space for HEAs.

In parallel to the development of ANN models, the MC/MD simulation results are also used to investigate the underlying mechanisms of segregation in HEAs and develop a surrogate model (DBAM), which will be discussed in the next three sections.

New GB segregation phenomena in HEAs: A starting example

To illustrate the possible existence of new GB segregation phenomena unique to HEAs, we have conducted and analyzed MC/MD simulations of nine representative equimolar ternary (medium-entropy) to quinary (high-entropy) alloys, including: FeCoNi, CrMnNi, CrMnFe, CrFeNi, CrCoFe, CrFeCoNi, CrMnFeNi, CrMnFeCo, and CrMnFeCoNi.

As one interesting discovery, we find that the site competition in ordered GBs can lead to weak segregation in ternary alloys, while segregation of multiple elements coupled with GB disordering can induce strong co-segregation in quinary alloys (Fig. 3a, b). Specifically, the MC/MD-simulated GB structure of the CrMnNi ternary alloy at 1000 K (Fig. 3c) shows that the relatively ordered GB (Γ_{Dis} of $\sim 39 \text{ nm}^{-2}$) has weak segregation of Cr and virtually no segregation of Mn ($\Gamma_{\text{Cr}} = 5.3 \text{ nm}^{-2}$ and $\Gamma_{\text{Mn}} = 0.8 \text{ nm}^{-2}$). However, the more disordered GB (Γ_{Dis} of $\sim 43 \text{ nm}^{-2}$) in CrMnFeCoNi exhibits strong co-segregation of Cr and Mn ($\Gamma_{\text{Cr}} = 18.6 \text{ nm}^{-2}$ and $\Gamma_{\text{Mn}} = 7.0 \text{ nm}^{-2}$). The compositional profiles shown in Fig. 3c, d confirm the strong GB segregation of both Cr and Mn in CrMnFeCoNi, but weak GB segregation in CrMnNi. Moreover, the computed profile of the disorder parameter also verifies a more disordered GB core of $\sim 0.88 \text{ nm}$ thick in CrMnFeCoNi vs. a less disordered GB core of $\sim 0.75 \text{ nm}$ thick in CrMnNi.

It is interesting to further note that for the systems without Mn element (*e.g.*, CrCoFe and CrFeCoNi), Cr atoms are not favorable to segregate at relatively ordered GBs (Supplementary Fig. S5). The structural analysis based on polyhedral template matching (PTM) approach³¹ shows that Mn segregation can induce significant GB disordering (Supplementary Fig. S7). Since disordered GB can prompt segregation, our observation suggests that the Cr segregation is enhanced by Mn-segregation induced GB disordering. See Supplementary Discussion 4 for more results and further discussion of this set of nine representative equimolar alloys. Notably, all abovementioned phenomena can be also found in other ternary, quaternary, and quinary systems, thereby suggesting the generality of the coupling effects.

Correlation analysis for GB properties

We further analyze the correlations between GB adsorption (i.e., Γ_{Cr} , Γ_{Mn} , Γ_{Fe} , Γ_{Co} , and Γ_{Ni}) and structural properties (Γ_{Dis} and V_{Free}) by calculating the Pearson correlation coefficients (PCCs) based on the MC/MD-simulated dataset. The heat map of PCC shows that GB disorder is strongly correlated with GB adsorption properties. However, there is almost no correlation between GB free volume (V_{Free}) with others. Specifically, the segregation of Mn (Γ_{Mn}) has the strongest correlation with GB disorder (Γ_{Dis}) among all elements, which agree with the MC/MD simulations showing that Mn segregation can induce large GB disordering. In addition, by calculating the PCCs at different temperatures, we found that the correlations between GB disorder and adsorption properties decrease with increasing temperature, while the correlations between other GB properties remain almost unchanged. The correlation analysis (elaborated in Supplementary Discussion 5) further verifies the importance of interfacial disordering on GB segregation in HEAs.

Next, we examine the correlation of Γ_i vs. Γ_{Dis} at different temperatures. Linear regression analyses (see Fig. 4c for Γ_{Cr} vs. Γ_{Dis} as an example and all six cases in Supplementary Fig. S10a-e) show the following statistical relations:

$$\Gamma_i(T, X) - \Gamma_i^0 = \bar{\alpha}_{\text{Dis}}^i(T) \cdot [\Gamma_{\text{Dis}}(T, X) - \Gamma_{\text{Dis}}^0], \quad (1a)$$

where T is temperature, $X = \{X_i\}$ is the bulk composition, $(\Gamma_i^0, \Gamma_{\text{Dis}}^0)$ is the intersection point of all linear regression lines that is virtually independent of temperature, and $\bar{\alpha}_{\text{Dis}}^i(T)$ is the slope. Interestingly, excellent linear correlations exist for $\bar{\alpha}_{\text{Dis}}^i$ vs. T for all elements (Fig. 4d):

$$\bar{\alpha}_{\text{Dis}}^i(T) = \beta_i \cdot (T - T_C), \quad (1b)$$

where β_i is the slope. Notably, the linear regression lines of $\bar{\alpha}_{\text{Dis}}^i$ vs. T for all five elements cross over at nearly the same point on the T axis (Fig. 4d), which is denoted as T_C ($\sim 1388 \pm 51$ K). The physical meaning and origin of T_C will be discussed subsequently in the next section and further elaborated in Supplementary Discussion 12.

Taking Cr as one example, Fig. 4c shows that the MC/MD-simulated Γ_{Cr} has linear relation with Γ_{Dis} statistically. The positive slopes ($\bar{\alpha}_{\text{Dis}}^{\text{Cr}} > 0$) of the Γ_{Cr} vs. Γ_{Dis} regression lines are related to the positive Cr segregation at the GB. The fitted $\bar{\alpha}_{\text{Dis}}^{\text{Cr}}$ value linearly decays by increasing the temperature with a negative slope of β_{Cr} , and intersects with the T axis at $T_C = 1347$ K (Fig. 4d).

Similar behavior can also be found for Mn (with moderate positive GB segregation), where $\bar{\alpha}_{\text{Dis}}^{\text{Mn}} > 0$ (Supplementary Fig. S10), $\beta_{\text{Mn}} < 0$, and $T_C = 1464$ K (albeit high uncertainty in T_C due to the small slope; Fig. 4d). In contrast, the slopes of $\Gamma_{\text{Fe}(\text{Co})}$ vs. Γ_{Dis} regression lines are negative ($\bar{\alpha}_{\text{Dis}}^{\text{Fe}(\text{Co})} < 0$) due to the depletion of Fe or Co (Supplementary Fig. S10); consequently, $\bar{\alpha}_{\text{Dis}}^{\text{Fe}(\text{Co})}$ linearly increases with increasing temperature ($\beta_{\text{Fe}(\text{Co})} > 0$; $T_C = 1370$ K for Fe and 1371 K for Co, respectively, in Fig. 4d).

A data-based analytical model (DBAM)

We propose a DBAM as a surrogate model based on the MC/MD-simulated data, particularly the linear correlations represented by equations. (1a) and (1b) and shown in Figs. 4C-D (and Supplementary Fig. S10). The detailed derivation and data-fitting of this DBAM can be found in Supplementary Discussion 6, with a brief discussion here. First, we express the GB excess of disorder as:

$$\Gamma_{\text{Dis}}(T, X) = \Gamma_{\text{Dis},0}(X) \cdot \exp\left(-\frac{E_{\text{A}}^{\text{Dis}}}{k_{\text{B}}T}\right). \quad (2a)$$

where $E_{\text{A}}^{\text{Dis}}$ is an activation energy and k_{B} is the Boltzmann constant. We adopt a linear expression as a first-order approximation for temperature-independent pre-factor: $\Gamma_{\text{Dis},0}(X) = \sum_i (\kappa_i^{\text{Dis}} \cdot X_i)$, where κ_i^{Dis} is the compositional coefficients for GB disorder. By using the fitted parameters listed in Supplementary Table S1, a good linear relation between predicted Γ_{Dis} and MC/MD values is found (with a small RMSE value of $\sim 2.3 \text{ nm}^{-2}$; Supplementary Fig. S11), thereby supporting the validity of the proposed equation (2a) and the linear expansion of the pre-factor.

Second, based on equations. (1a), (1b), and (2a), we can express the GB excess of solute i as:

$$\Gamma_i(T, X) - \Gamma_i^0(X) = \Delta\Gamma_{\text{Dis}}(T, X) \cdot \beta_i \cdot (T - T_C), \quad (2b)$$

where $\Delta\Gamma_{\text{Dis}} \equiv [\Gamma_{\text{Dis}}(T, X) - \Gamma_{\text{Dis}}^{\text{min}}]$ is the increased GB disorder induced by segregation and/or temperature from its minimum level of $\Gamma_{\text{Dis}}^{\text{min}}$ ($\approx \Gamma_{\text{Dis}}^0$ in equation (1)). In equation (2b), the compositionally-dependent $\Gamma_i^0(X)$ replaces the constant Γ_i^0 ($\approx \langle \Gamma_i^0(X) \rangle$) in equation (1a) for more accurate fitting. Here, we again adopt a linear approximation: $\Gamma_i^0(X) = \sum_j (\kappa_{i,j}^{\text{Seg}} \cdot X_j)$, where $\kappa_{i,j}^{\text{Seg}}$ is a compositional coupling coefficient for the GB segregation.

The fitted κ_i^{Dis} and $\kappa_{i,j}^{\text{Seg}}$ values listed in Supplementary Tables S1 and S2 represent the couplings between segregation and disorder, as well as segregation of different elements, which are fully consistent with the trends observed in our MC/MD simulations, as discussed in Supplementary Discussion 6. Notably, we can predict the $\Gamma_i(T, X)$ with relatively small RMSEs (albeit slightly larger than those from the ANN predictions) for each element using this simple analytical equation (see equations. (2a) and (2b)), as shown in Supplementary Table S2. Furthermore, the parity plots show that the DBAM predictions agree well with the MC/MD simulations for all elements (Supplementary Fig. S11).

This DBAM provides a new physics insight via decoupling the effect of GB disorder on segregation, which is further discussed as follows. The term $\Gamma_i^0(X)$ in equation (2b) is the composition contribution to the GB adsorption at the minimum disorder, while $\Delta\Gamma_{\text{Dis}}(T, X) \cdot \beta_i \cdot (T - T_C)$ represents the influence of disorder (called “disorder contribution” for brevity here, albeit it is a coupled disorder and segregation effect). Thus, we can further calculate the fractions of disorder contribution to the 1032 model-predicted Γ_i values and plot them in a histogram for all five elements in Fig. 5a. The large fractions of 0.70 for Γ_{Cr} , 0.71 for Γ_{Fe} , and 0.66 for Γ_{Co} , respectively, suggest the significant roles of GB disorder in influencing the segregation of Cr, Fe, and Co. However, the fractions of disorder contributions are moderate (~ 0.46) for Γ_{Mn} and almost zero for Γ_{Ni} (Fig. 5a). Interestingly, the fraction of disorder contribution is proportional to the absolute value of coupling coefficient $|\beta_i|$. Thus, these findings demonstrate the importance of GB disorder on influencing GB segregation in HEAs, particularly for Cr, Fe, and Co in this case.

The physical meaning and origin of T_C are further discussed in Supplementary Discussion 12 and briefly summarized here. The equation (2b) implies that at $T = T_C$, $\Gamma_i(T_C, X) = \Gamma_i^0(X)$, which is a small number (because $\Gamma_i^0 = \langle \Gamma_i^0(X) \rangle$ is small as shown in Fig. 4c and Supplementary Fig. S10). This can also be derived from the statistical analysis shown Fig. 5a, which suggest that $\Gamma_i^0(X)$ contributes only small fractions to $\Gamma_i(T, X)$ for any strong segregating/depleting elements (and it should also be small for any weak segregating/depleting elements). Thus, T_C represents the compensation temperature at which the effective GB segregation entropy ($\Delta S_{i \rightarrow 1}^{\text{Seg (eff)}}$, where the subscript “ $i \rightarrow 1$ ” denotes the swap of an i atom in the bulk and reference 1 atom at GB) is proportional to the effective GB segregation enthalpy ($\Delta H_{i \rightarrow 1}^{\text{Seg (eff)}}$) to produce $\Gamma_i(T_C, X) \sim 0$:

$$\Delta S_{i \rightarrow 1}^{\text{Seg (eff)}} = \frac{\Delta H_{i \rightarrow 1}^{\text{Seg (eff)}}}{T_C}. \quad (3)$$

Comparing with equation (2b), we conclude that this entropic effect must be related to the increased GB disorder $\Delta \Gamma_{Dis}$. Thus, we can now envision the following picture for the physical meaning and origin of T_C . The increased GB disorder $\Delta \Gamma_{Dis}$ can reduce the effective GB free energy of segregation ($\Delta G_{i \rightarrow 1}^{\text{Seg (eff)}} = \Delta H_{i \rightarrow 1}^{\text{Seg (eff)}} - T \cdot \Delta S_{i \rightarrow 1}^{\text{Seg (eff)}}$) through the entropy of GB segregation, where the reduction is proportional to $\Delta H_{i \rightarrow 1}^{\text{Seg (eff)}}$ and more significant for strong segregating or depleting element. Thus, with increasing GB disorder $\Delta \Gamma_{Dis}$, GB segregation (or depletion) for different elements are reduced and equalized due to this entropic effect. The effective $\Delta G_{i \rightarrow 1}^{\text{Seg (eff)}}$ virtually vanishes (or is minimized in reality) at this compensation temperature T_C . It should be noted that this compensation effect is likely only an approximated relation (because $\Gamma_i(X)$ is small but not exactly zero and equation (3) is likely an approximation). Our data (Fig. 4d and Supplementary Table S2) also show variations in the best fitted T_C values for different elements (with a mean of 1388 K and a standard deviation of 51 K). We should also note that this predicted T_C is from an extrapolation. As the temperature approaches the bulk solidus curve, premelting-like interfacial phases^{6,28,32,33} can develop at GBs to change the projection.

It is interesting to further compare the fitted compositional coefficients ($\kappa_{i,j}^{\text{Seg}}$) with the corresponding segregation enthalpies in binary alloys. Also taking Cr as one example, Fig. 5b shows the parity plot of Cr segregation enthalpies $\Delta H_{Cr,j}^{\text{Seg}}$ ($j = \text{Mn, Fe, Co, Ni}$) vs. corresponding coupling coefficients $\kappa_{i,j}^{\text{Seg}}$, where an excellent linear relation with $R^2 = 0.949$ indicates a strong positive correlation. In addition, signs of the $\Delta H_{Cr,j}^{\text{Seg}}$ and $\kappa_{i,j}^{\text{Seg}}$ are always consistent. For instance, both a positive $\Delta H_{Cr,Fe}^{\text{Seg}}$ (or $\Delta H_{Cr,Ce}^{\text{Seg}}$) in the classical segregation model and a positive $\kappa_{Cr,Fe}^{\text{Seg}}$ (or $\kappa_{Cr,Co}^{\text{Seg}}$) in our DBAM indicate preferred segregation of Cr at the GB of Fe (or Co). Likewise, negative $\Delta H_{Cr,Mn}^{\text{Seg}}$ (or $\Delta H_{Cr,Ni}^{\text{Seg}}$) and $\kappa_{Cr,Mn}^{\text{Seg}}$ (or $\kappa_{Cr,Ni}^{\text{Seg}}$) suggest preferred depletion of Cr at the GB of Mn (or Ni). Thus, the compositional coefficients ($\kappa_{i,j}^{\text{Seg}}$) are well correlated with binary segregation enthalpies.

Comparisons with classical and other existing segregation models

Here, we further compare the MC/MD-simulated GB segregation in HEAs with segregation predicted by classical or other existing segregation models.

First, GB segregation in HEAs can exhibit more complex and intriguing behaviors than those in binary alloys. Here, we adopt the Wynblatt-Ku model³⁴ (considering both chemical and elastic contribution to GB segregation; see Supplementary Discussion 7) to compute GB fractions (X_{GB}) of Cr as functions of bulk fractions of Cr ($x = X_{Cr}$) for four Cr_xM_{1-x} ($M = Mn, Fe, Co, Ni$) binary alloys at 1000 K (Fig. 5c). Then, we select four HEAs, including $Cr_xMn_{0.4-x}Fe_{0.2}Co_{0.2}Ni_{0.2}$ ($0.05 \leq x \leq 0.35$), as well as three variants where we swap Mn with Fe, Co, or Ni; we further plot MC/MD-simulated Γ_{Cr} curves as functions of x in Fig. 5d. We notice several major differences in the trends of segregation in binary alloys *vs.* HEAs. The segregation strengths of Cr in binary alloys are ranked as $Fe > Co > Ni > Mn$ (Fig. 5c), while they are ranked as $Mn \approx Ni > Co \approx Fe$ in HEAs (Fig. 5d). More complex and intriguing compositional dependences, *e.g.*, saturation of Cr segregation with $x > 0.2$ in $Cr_xMn_{0.2}Fe_{0.4-x}Co_{0.2}Ni_{0.2}$ and $Cr_xMn_{0.2}Fe_{0.2}Co_{0.4-x}Ni_{0.2}$ *vs.* acceleration of Cr segregation after $x > 0.2$ in $Cr_xMn_{0.2}Fe_{0.2}Co_{0.2}Ni_{0.4-x}$, are also observed in HEAs (Fig. 5d).

Second, Li *et al.* recently proposed a density-based thermodynamic model for GB segregation in CrMnFeCoNi²³. This phenomenological model assumed that GB energy can be written a function of GB density, which suggested the importance of GB free volume (V_{Free}). However, the PCC heat map (Fig. 4a) shows that V_{Free} almost has no correlations with GB adsorption properties (Γ_i). Instead, Γ_{Dis} exhibits strong correlation with Γ_i (Fig. 4a). Thus, we suggest that GB disorder (instead of density or free volume) should be treated as a key parameter for developing future phenomenological models. See Supplementary Discussion 8 for further discussion.

Third, we have extended a lattice-type model developed by Xing *et al.* for ternary alloys³⁵ to quinary HEAs in Supplementary Discussion 9. Although this model can predict some general trends, *e.g.*, the positive segregation enthalpies for Cr, Mn, and Ni (segregation) *vs.* negative segregation enthalpies for Fe and Co (depletion), we cannot make quantitative predictions of GB segregation for non-equi-molar HEAs. See Supplementary Discussion 9 and Supplementary Figs. S12-S14 for elaboration.

Generality of the predictions

In this study, the majority of MC/MD simulations are based on an asymmetric $\Sigma 81$ (mixed tilt and twist) GB to represent the behaviors of general GBs. To test generality of our predictions, we

have also performed MC/MD simulations for three other GBs, including an asymmetric $\Sigma 15$ (mixed tilt and twist) GB, a $\Sigma 41$ symmetric tilt GB, and a $\Sigma 13$ symmetric twist GB. For each of them, four non-equimolar HEAs selected based in the simulations of the asymmetric $\Sigma 81$ GB diagrams, where the first three (HEA1-3) exhibit strong Cr segregation while last one (HEA4) has weak Cr segregation, were examined. Notably, MC/MD simulations show similar and consistent trends for all four GBs: HEA1-3 always have large Γ_{Cr} , but HEA4 always has small Γ_{Cr} (Supplementary Table S4 and Supplementary Fig. S15). Furthermore, DFT calculations also confirm that $E_{\text{Seg}}^{\text{Cr}}$ (around -0.026 eV/atom) of HEA1-3 is significantly lower than that for HEA4 (~ 0.0001 eV/atom), as shown in Supplementary Table S4. See Supplementary Discussion 10 for further discussion of the results of these four different GBs. In conclusion, the trends predicted based on the asymmetric $\Sigma 81$ (mixed tilt and twist) GB are likely representative.

First-principles calculations of electronic structures of HEAs

We have also calculated sum of bond ordering (SBO) values for the four non-equimolar HEAs discussed above to further understand how the bonding environment affects the Cr segregation (see Methods). Since SBO represents the total number of electrons that form bonds, similar SBO values indicate similar bonding environments. Interestingly, Fe, Cr, and Co atoms always have similar SBO values, which are ~ 4.04 , ~ 3.95 , and ~ 3.78 , respectively. In contrast, Mn and Ni exhibit two distinct SBO values of ~ 4.20 and ~ 3.49 , respectively (Supplementary Fig. S16). Therefore, the preferred Cr segregation at the Fe- or Co-rich GBs can be understood because Fe or Co can provide more favorable segregation sites with similar bonding environments. On the other hand, the different bonding environments at Mn- or Ni-rich GBs can inhibit Cr segregation.

A recent study suggested that SBO can be used as a descriptor to predict and subsequently tailor GB segregation²⁷. For example, if we want to promote segregation of a certain element (*e.g.*, Cr) in HEAs, we can increase the composition of the elements with similar SBO values (*e.g.*, Fe and Co) and/or reduce the composition of those with different SBO values (*e.g.*, Mn and Ni).

Conclusions

Via using hybrid MC/MD simulations and careful correlation analyses, we reveal the (previously unrecognized) importance of couplings the segregation of multiple elements and GB disordering in HEAs. Both ANN models and a surrogate data-based analytical model (DBAM) have been developed to predict GB adsorption properties as functions of temperature and bulk

compositions in a 5D space. The dataset generated in this work with 1032 MC/MD simulations represents the largest dataset for GB segregation in HEAs to date. Our data-based model further predicts the existence of a compensation temperature at which GB segregation should be minimized. This study not only opens a new paradigm to explore the vast compositional space of HEAs, but also expands our fundamental knowledge on GB segregation theory.

Methods

Composition Selection and Principal Component Analysis. In this work, the composition of each element was fixed in a range from 5 at% to 35 at% with a step of 5 at% for $\text{Cr}_x\text{Mn}_y\text{Fe}_z\text{Co}_l\text{Ni}_m$. Since $x + y + z + l + m = 1$, there are 1371 possible compositions in total. Among them, we randomly selected 258 subsystems to perform high-throughput MC/MD simulations to generate a dataset. Principle component analysis (PCA) was used to analyze the composition distribution for these 258 subsystems to ensure the randomness of our selection, where the singular value decomposition (SVD) algorithm was chosen. The PCA were performed by Matlab2019a.

Hybrid MC/MD simulation for GB diagrams. The GBstudio³⁶ website was used to construct a mixed twist-tilt $\Sigma 81$ GB with boundary planes $(1\bar{1}0)/(7\bar{8}7)$ to represent general GBs. The energy minimization for each GB was first performed at 0 K by conjugate gradient (CG) algorithm. Subsequently, the hybrid Monte Carlo and molecular dynamics (hybrid MC/MD) simulations in constant NPT ensembles were carried out to swap atoms and find energetically favorable GB structure. Five MC trial moves were conducted between each MD step with a 0.1 fs MD time step and 10^5 hybrid MC/MD steps performed for each simulation to achieve convergence. All MC/MD simulations were performed using the LAMMPS code³⁷. A 2NN MEAM potential³⁸ was adopted for CrMnFeCoNi alloys.

The methods used to calculate GB excess of solute (*i.e.*, GB adsorption amount Γ_{Cr} , Γ_{Mn} , Γ_{Fe} , Γ_{Co} , Γ_{Ni}) and disorder (Γ_{Dis}) diagrams were same as our prior studies; the detailed procedures are described in Refs.^{20,27}. To calculate GB free volume (V_{Free}), we used the relation of $V_{\text{Free}} = V_{\text{Total}} \cdot \sum \Gamma_i$, where V_{Total} is the total volume of GB structure and $i = \text{Cr, Mn, Fe, Co, or Ni}$.

It should be noted that we set an overall global composition in a hybrid MC/MD simulation. The bulk composition is recalculated based the grain composition (away from the GB region) after achieving the chemical equilibrium, which is subsequently used for both training the ANN model and further analysis and developing a data-based analytical model.

Artificial neural networks. The data set was divided into training, validation, and test subsets in a ratio of 0.7:0.15:0.15. The Levenberg-Marquardt backpropagation function was adopted to train ANN models. We found the optimized network architectures for the ANN ($n^i - n^{[i]} - 1$, where n^i is the number of input parameter, $n^{[i]}$ (the number of neurons in the single layer) is set to be 6-20-1. All data processing and ANN development were performed by Deep Learning Toolbox in Matlab2019a.

Density function theory (DFT) calculations. The first-principles DFT calculations were performed by using the Vienna *ab initio* Simulations Package (VASP)^{39,40}. The Kohn-Sham

equations were used to solve the projected-augmented wave (PAW) method^{41,42} along with standard PAW potentials. All GB structures were fully relaxed until the Hellmann-Feynman forces were smaller than 0.02 eV/Å. The Brillouin-zone integrations were sampled on a Γ -centered $2\times 2\times 1$ k -point grids. The kinetic energy cutoff for plane waves was set to 368 eV. The convergence criterion for the electronic self-consistency was set to 10^{-4} eV. The “high” precision setting was adopted to avoid wrap around errors. The spin-polarization was not considered due to weak effect on atomic arrangement⁴³. The SBO was calculated by using the state-of-the-art DDEC06 method⁴⁴ following the all-electron static calculations.

Acknowledgements: This work is currently supported by the UC Irvine MRSEC, Center for Complex and Active Materials, under National Science Foundation award DMR-2011967 partially. We also acknowledge the earlier support from a Vannevar Bush Faculty Fellowship sponsored by the Basic Research Office of the Assistant Secretary of Defense for Research and Engineering and funded through the Office of Naval Research under Grant No. N00014-16-2569, prior to the establishment of the MRSEC. The calculations were performed at the Triton Shared Computing Cluster (TSCC) at the University of California, San Diego (UCSD).

Author contributions: J. L. conceived the idea and supervised the work. C. H. performed simulations and calculations. Both authors wrote, reviewed, and revised the manuscript.

Competing interests: The authors declare no conflict of interests.

Data availability: The well-trained ANN models are available on GitHub website. The original MC/MD data are upon request from authors.

Supplementary Information:

Supplementary Discussions 1-12

Supplementary Tables S1-S4

Supplementary Figs. S1–S29

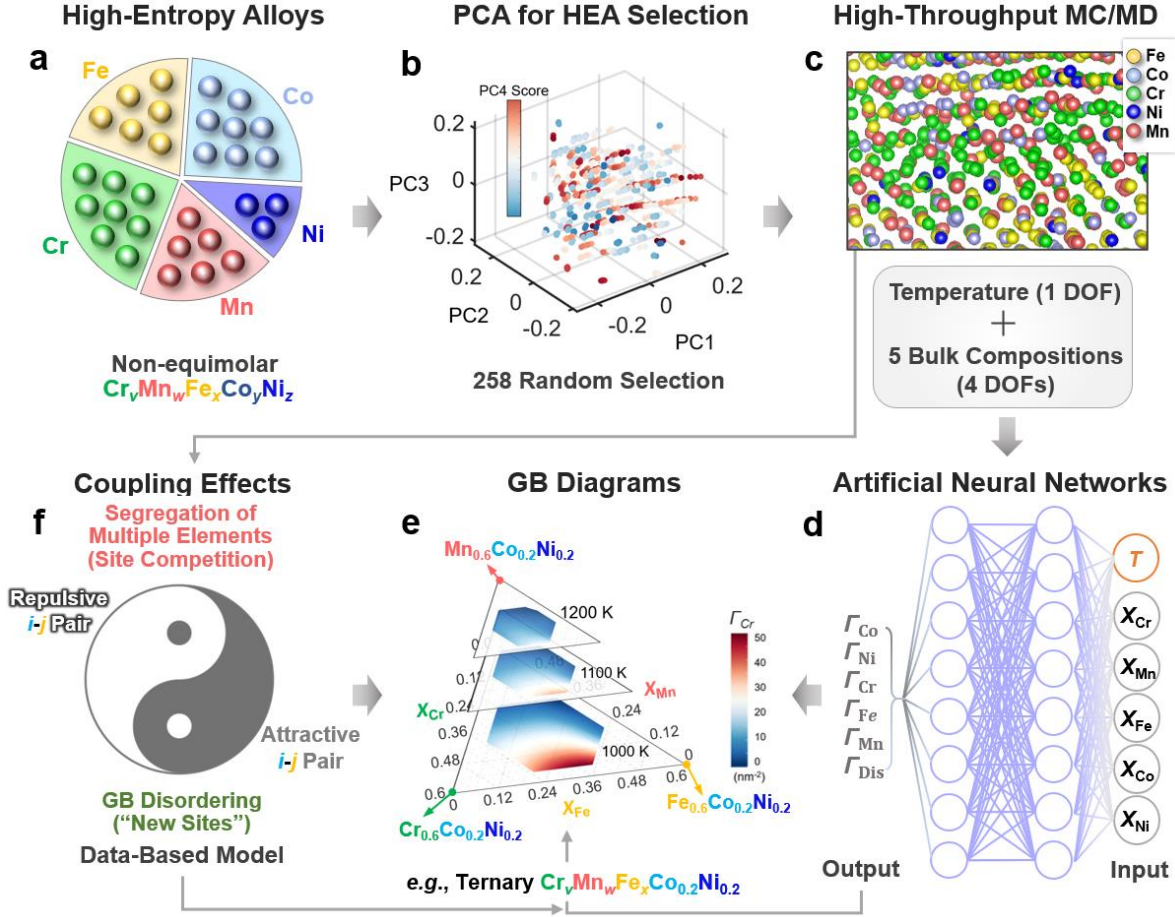


Fig. 1. Workflow of machine learning prediction of grain boundary (GB) properties for high-entropy alloys (HEAs), further in-depth correlation analyses to reveal underlying mechanisms, and development of a surrogate data-based analytical model (DBAM). **a**, Schematic diagram of non-equimolar five-element $\text{Cr}_x\text{Mn}_y\text{Fe}_z\text{Co}_l\text{Ni}_m$ alloys. **b**, Principal component analysis (PCA) verifying the randomness in the selection of 258 HEAs. **c**, the equilibrium structure of an asymmetric $\Sigma 81$ GB in $\text{Co}_{0.2}\text{Ni}_{0.2}\text{Cr}_{0.2}\text{Fe}_{0.35}\text{Mn}_{0.05}$ at 1000 K obtained by isothermal-isobaric (constant NPT) ensemble hybrid Monte Carlo and molecular dynamics (hybrid MC/MD) simulations. In total, 1032 such individual hybrid MC/MD simulations were performed for 258 HEAs at four different temperatures to calculate GB excesses of solutes (*i.e.*, $\Gamma_{\text{Cr}}, \Gamma_{\text{Mn}}, \Gamma_{\text{Fe}}, \Gamma_{\text{Co}}, \Gamma_{\text{Ni}}$) and disorder (Γ_{Dis}), and free volume (V_{Free}). **d**, Schematic diagram of an artificial neural networks (ANN) with a 6-20-1 architecture for predicting six GB properties. This ANN model, which was trained based on 1032 individual hybrid MC/MD simulations, can predict the six GB properties as functions of the bulk compositions and temperature in a 5D space. **e**, An example of GB diagrams predicted by the ANN model for a ternary $\text{Cr}_x\text{Mn}_y\text{Fe}_z\text{Co}_{0.2}\text{Ni}_{0.2}$ ($x + y + z = 0.6$) subsystem, showing three isothermal sections of the Cr adsorption (Γ_{Cr}) diagrams. **f**, We also used hybrid MC/MD simulation results to investigate the couplings of the segregation of multiple elements and GB disordering in HEAs. Subsequently, a surrogate DBAM was developed based on the MC/MD-simulated data to predict GB properties and reveal complex segregation behaviors in HEAs that cannot be captured by the classical thermodynamic models.

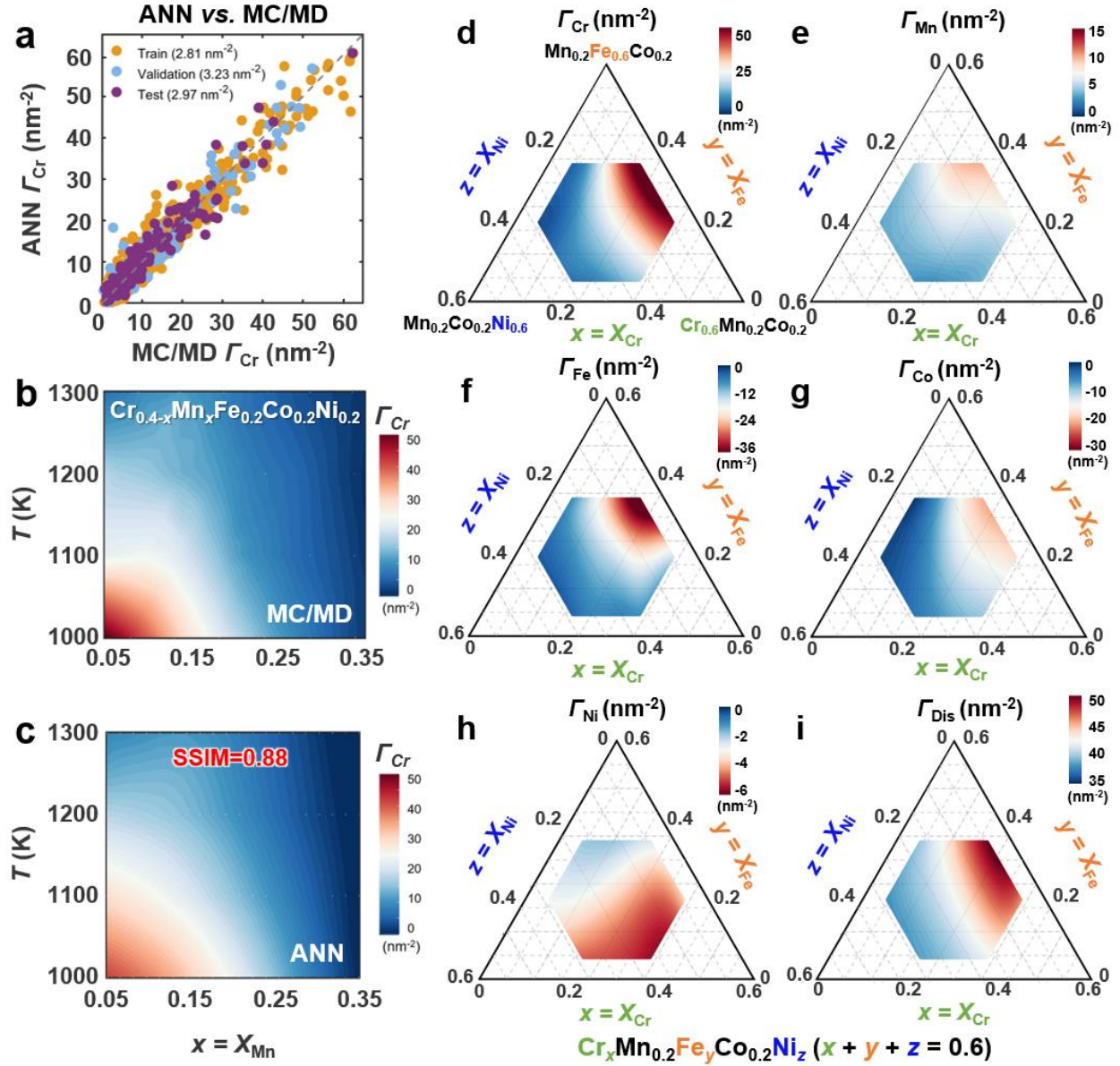


Fig. 2. ANN performance for predicting GB properties. **a**, Parity plot of ANN predictions vs. MC/MD simulations for the GB excess of Cr adsorption (Γ_{Cr}). **b**, **c**, MC/MD-simulated vs. ANN-predicted isopleths of Γ_{Cr} diagrams as functions of temperature and Mn bulk composition ($x = X_{Mn}$) for the $Cr_{0.4-x}Mn_xFe_{0.2}Co_{0.2}Ni_{0.2}$ system. **d-i**, Representative ternary isothermal sections of ANN-predicted GB diagrams of Γ_{Cr} , Γ_{Mn} , Γ_{Fe} , Γ_{Co} , Γ_{Ni} , and Γ_{Dis} for $Cr_xMn_{0.2}Fe_yCo_{0.2}Ni_z$ ($x + y + z = 0.6$; $x = X_{Cr}$, $y = X_{Fe}$, $z = X_{Ni}$) at 1000 K.

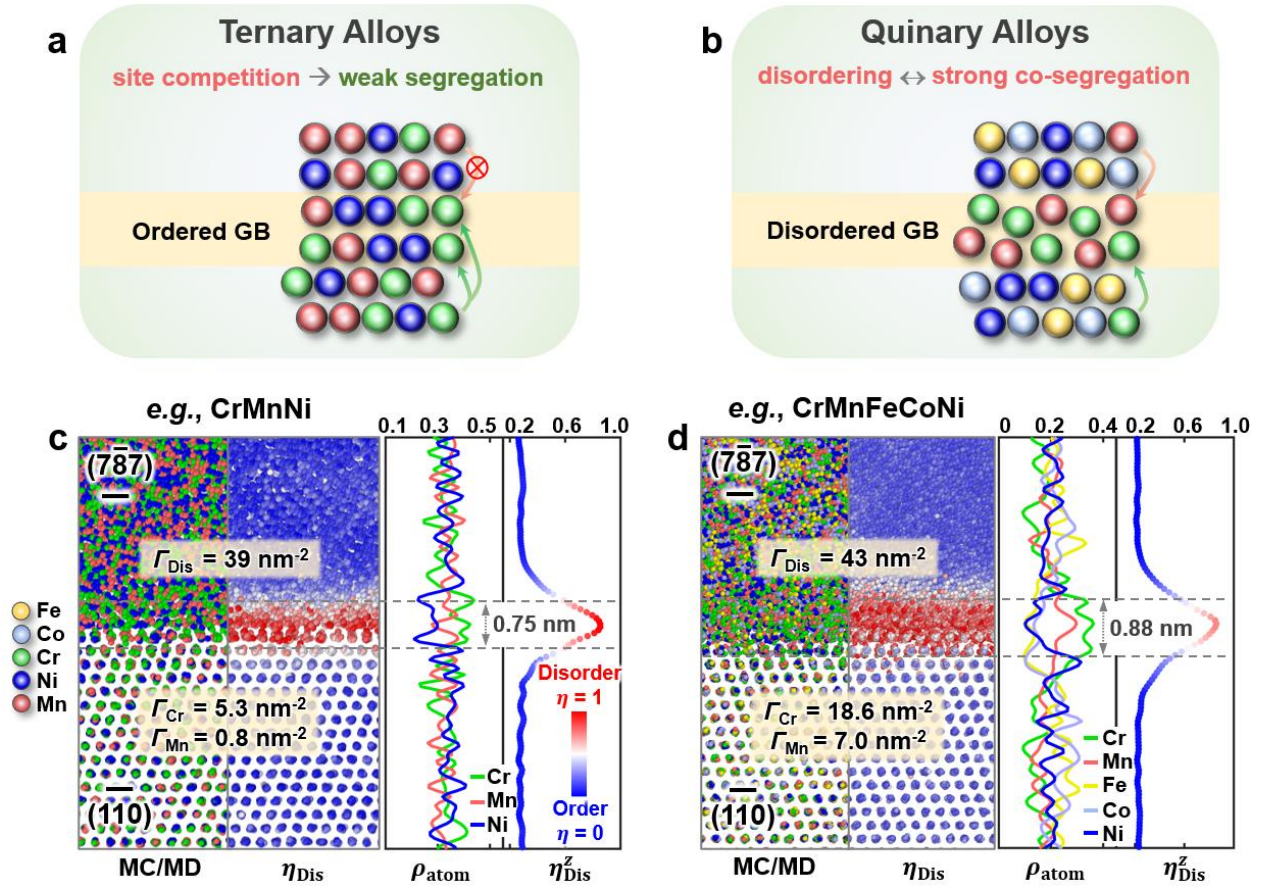


Fig. 3. Unique coupled interfacial disordering and GB co-segregation behaviors in HEAs, exemplified by comparing the same asymmetric $\Sigma 81$ GB in equimolar CrMnNi vs. CrMnFeCoNi alloys at 1000 K. **a**, Schematic of weak segregation in ternary alloys ascribed to the site competition in relatively ordered GBs. **b**, Schematic of the coupling of interfacial disordering and strong co-segregation of multiple elements in quinary alloys. **c**, MC/MD-simulated GB structure of the equimolar CrMnNi alloy and the corresponding disorder parameter (η_{Dis}) and atomic density profiles. This GB exhibits an GB excess disorder Γ_{Dis} of $\sim 39 \text{ nm}^{-2}$, moderate segregation of Cr ($\Gamma_{Cr} = \sim 5.3 \text{ nm}^{-2}$), and weak segregation of Mn ($\Gamma_{Mn} = \sim 0.8 \text{ nm}^{-2}$). **d**, MC/MD-simulated GB structure of the equimolar CrMnFeCoNi and the corresponding disorder parameter (η_{Dis}) and atomic density profiles. In comparison with the same GB in the ternary CrMnCr alloy, this GB in the quinary Cantor alloy is more disordered with a larger Γ_{Dis} of $\sim 43 \text{ nm}^{-2}$ and strong co-segregation of Cr and Mn ($\Gamma_{Cr} = \sim 18.6 \text{ nm}^{-2}$ and $\Gamma_{Mn} = \sim 7.0 \text{ nm}^{-2}$, which represent $\sim 3.5\times$ and $\sim 9\times$ increases, respectively, from those in the ternary alloy). More examples and further discussion can be found in Supplementary Discussion 4.

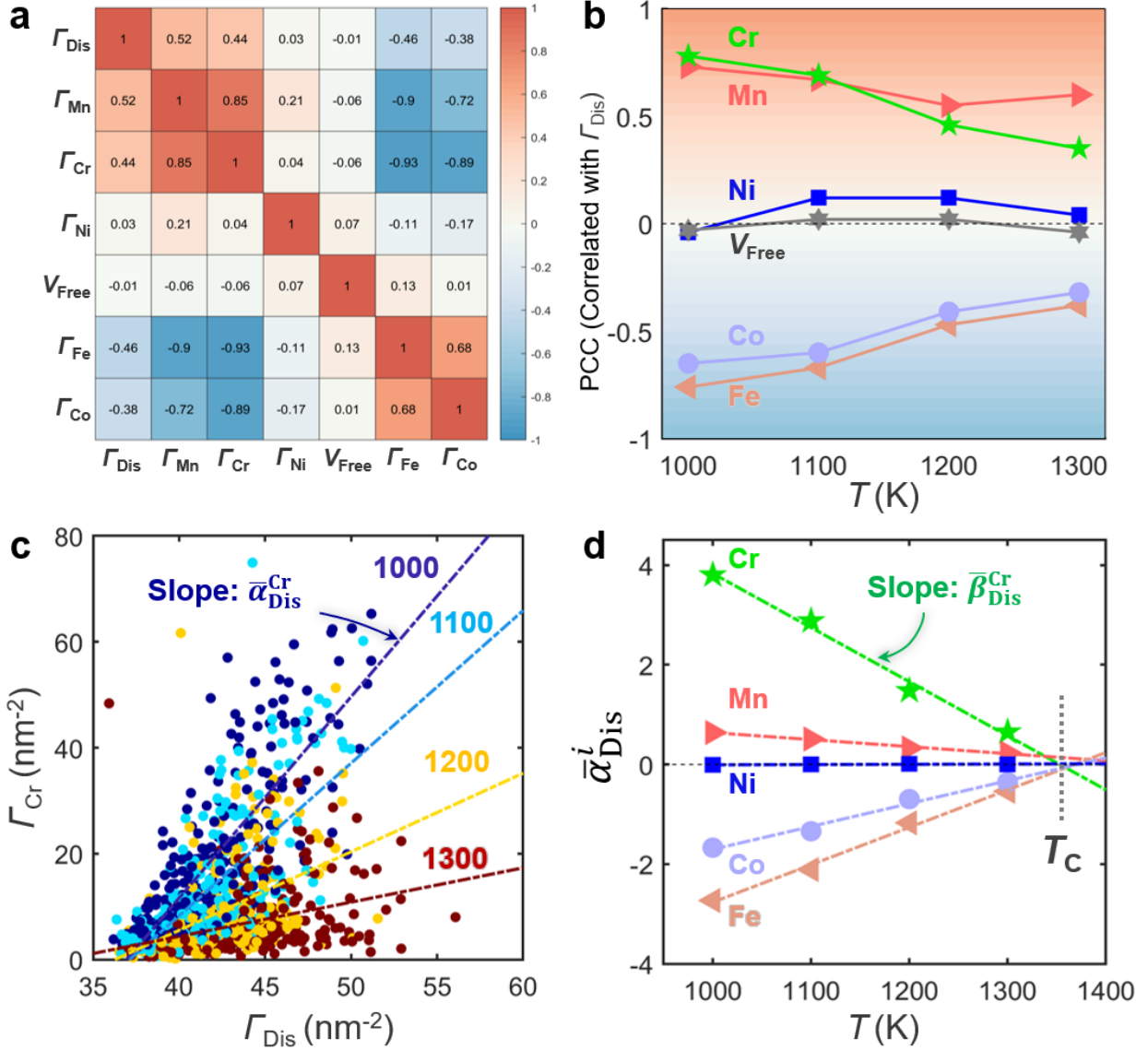


Fig. 4. Correlation analyses of GB properties. **a**, Heat map of Pearson correlation coefficients (PCCs) between all pairs of the seven GB properties. **b**, Calculated correlation coefficients between GB excess of disorder (Γ_{Dis}) and six other GB properties (GB excesses of Cr, Fe, Co, Ni and Mn, as well as GB free volume) at different temperatures. **c**, Plot of GB excess of Cr (Γ_{Cr}) vs. GB excess of disorder (Γ_{Dis}) at 1000 K, 1100 K, 1200 K, and 1300 K, respectively. The dashed lines are regression lines of Γ_{Cr} vs. Γ_{Dis} at different temperatures based on 258 HEA compositions. Similar plots for all five elements can be found in Supplementary Fig. S10a-e. The slopes of these dashed lines are labelled as $\bar{\alpha}_{\text{Dis}}^i$, where $i = \text{Cr, Mn, Fe, Co, and Ni}$. **d**, The fitted $\bar{\alpha}_{\text{Dis}}^i$ as functions of temperature (T) for five elements. The slopes of $\bar{\alpha}_{\text{Dis}}^i$ vs. T regression lines are labelled as β_i . Notably, all five fitted linear lines cross over at nearly one point on T axis at $T_C \approx 1388 \pm 51$ K.

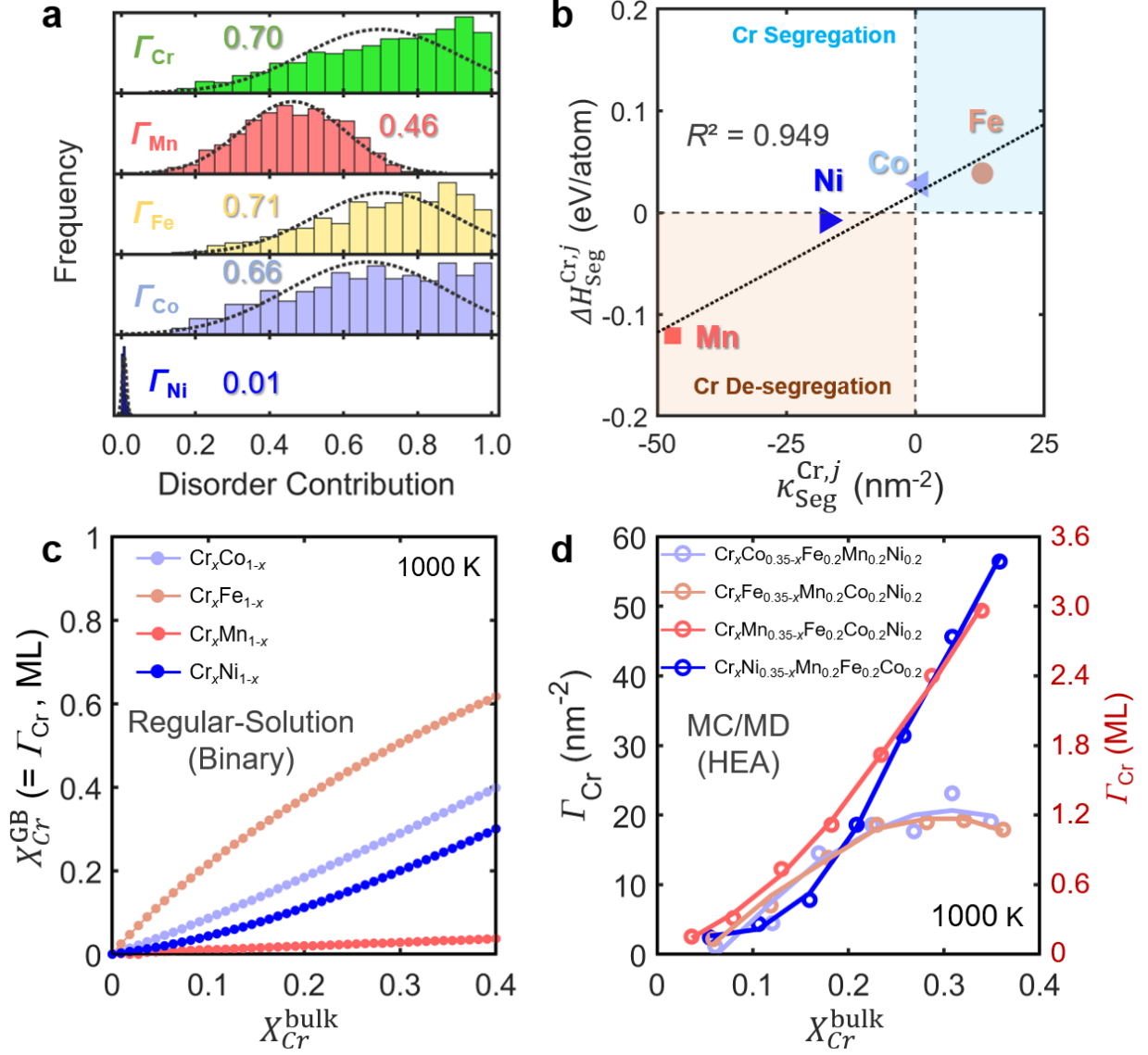


Fig. 5. Analyses and comparisons of the data-based analytical model (DBAM), classical segregation models, and MC/MD simulations. **a**, Histograms of the disorder contribution to GB adsorption of each element based on the DBAM. **b**, Parity plot of $\Delta H_{Cr,j}^{Seg}$ (the segregation enthalpy of Cr in the binary Cr- j alloy, where $j = Mn, Fe, Co,$ and Ni , calculated used a lattice-type model⁴⁵) vs. $\kappa_{Cr,j}^{Seg}$ (the compositional coupling coefficients in the DBAM). The positive (or negative) values of $\Delta H_{Cr,j}^{Seg}$ or $\kappa_{Cr,j}^{Seg}$ indicate Cr is favorable (or unfavorable) to segregate. **c**, Calculated GB adsorption ($X_{Cr}^{GB} = \Gamma_{Cr}$) vs. the bulk Cr fraction (X_{Cr}^{bulk}) for four Cr_xj_{1-x} ($j = Mn, Fe, Co,$ and Ni) binary alloys at 1000 K using the Wynblatt-Ku model³⁴. **d**, MC/MD-simulated Γ_{Cr} vs. X_{Cr}^{bulk} for four HEAs at 1000 K. The compositions are noted in the legend, where in each case the increase in the Cr fraction is compensated by one selected element while keeping the fractions of the three other elements as constant at 0.2.

References

- 1 Ye, Y. F., Wang, Q., Lu, J., Liu, C. T. & Yang, Y. High-entropy alloy: challenges and prospects. *Materials Today* **19**, 349-362, doi:https://doi.org/10.1016/j.mattod.2015.11.026 (2016).
- 2 Tsai, M.-H. & Yeh, J.-W. High-Entropy Alloys: A Critical Review. *Materials Research Letters* **2**, 107-123, doi:10.1080/21663831.2014.912690 (2014).
- 3 Miracle, D. B. & Senkov, O. N. A critical review of high entropy alloys and related concepts. *Acta Materialia* **122**, 448-511, doi:https://doi.org/10.1016/j.actamat.2016.08.081 (2017).
- 4 George, E. P., Raabe, D. & Ritchie, R. O. High-entropy alloys. *Nature Reviews Materials* **4**, 515-534, doi:10.1038/s41578-019-0121-4 (2019).
- 5 Dillon, S. J., Tang, M., Carter, W. C. & Harmer, M. P. Complexion: A new concept for kinetic engineering in materials science. *Acta Materialia* **55**, 6208-6218, doi:https://doi.org/10.1016/j.actamat.2007.07.029 (2007).
- 6 Cantwell, P. R. *et al.* Grain boundary complexions. *Acta Materialia* **62**, 1-48, doi:https://doi.org/10.1016/j.actamat.2013.07.037 (2014).
- 7 Dey, D. & Bradt, R. C. Grain Growth of ZnO during Bi₂O₃ Liquid-Phase Sintering. *Journal of the American Ceramic Society* **75**, 2529-2534, doi:10.1111/j.1151-2916.1992.tb05607.x (1992).
- 8 Nie, J., Chan, J. M., Qin, M., Zhou, N. & Luo, J. Liquid-like grain boundary complexion and sub-eutectic activated sintering in CuO-doped TiO₂. *Acta Materialia* **130**, 329-338, doi:https://doi.org/10.1016/j.actamat.2017.03.037 (2017).
- 9 Luo, J., Wang, H. & Chiang, Y.-M. Origin of Solid-State Activated Sintering in Bi₂O₃-Doped ZnO. *Journal of the American Ceramic Society* **82**, 916-920, doi:10.1111/j.1151-2916.1999.tb01853.x (1999).
- 10 Dillon, S. J., Tai, K. & Chen, S. The importance of grain boundary complexions in affecting physical properties of polycrystals. *Current Opinion in Solid State and Materials Science* **20**, 324-335, doi:https://doi.org/10.1016/j.cossms.2016.06.003 (2016).
- 11 Krause, A. R. *et al.* Review of grain boundary complexion engineering: Know your boundaries. *Journal of the American Ceramic Society* **102**, 778-800, doi:10.1111/jace.16045 (2019).
- 12 Hu, T., Yang, S., Zhou, N., Zhang, Y. & Luo, J. Role of disordered bipolar complexions on the sulfur embrittlement of nickel general grain boundaries. *Nature Communications* **9**, 2764, doi:10.1038/s41467-018-05070-2 (2018).
- 13 Westbrook, J. H. SEGREGATION AT GRAIN BOUNDARIES. *Metallurgical Reviews* **9**, 415-471, doi:10.1179/mtlr.1964.9.1.415 (1964).
- 14 McLean, D. Grain Boundaries in Metals. *Oxford, Clarendon Press* (1957).
- 15 Hondros, E. D. & Seah, M. P. The theory of grain boundary segregation in terms of surface adsorption analogues. *Metallurgical Transactions A* **8**, 1363-1371, doi:10.1007/BF02642850 (1977).
- 16 Pan, Z. & Rupert, T. J. Effect of grain boundary character on segregation-induced structural transitions. *Physical Review B* **93**, 134113, doi:10.1103/PhysRevB.93.134113 (2016).
- 17 Frolov, T., Divinski, S. V., Asta, M. & Mishin, Y. Effect of Interface Phase Transformations on Diffusion and Segregation in High-Angle Grain Boundaries. *Physical Review Letters* **110**, 255502, doi:10.1103/PhysRevLett.110.255502 (2013).
- 18 Frolov, T., Asta, M. & Mishin, Y. Segregation-induced phase transformations in grain boundaries. *Physical Review B* **92**, 020103, doi:10.1103/PhysRevB.92.020103 (2015).
- 19 Hu, C. & Luo, J. First-order grain boundary transformations in Au-doped Si: Hybrid Monte Carlo and molecular dynamics simulations verified by first-principles calculations. *Scripta Materialia* **158**, 11-15, doi:https://doi.org/10.1016/j.scriptamat.2018.08.017 (2019).
- 20 Yang, S., Zhou, N., Zheng, H., Ong, S. P. & Luo, J. First-Order Interfacial Transformations with a Critical Point: Breaking the Symmetry at a Symmetric Tilt Grain Boundary. *Physical Review Letters* **120**, 085702, doi:10.1103/PhysRevLett.120.085702 (2018).

- 21 Ming, K., Li, L., Li, Z., Bi, X. & Wang, J. Grain boundary decohesion by nanoclustering Ni and Cr separately in CrMnFeCoNi high-entropy alloys. *Science Advances* **5**, eaay0639, doi:10.1126/sciadv.aay0639 (2019).
- 22 Li, Y. J., Savan, A., Kostka, A., Stein, H. S. & Ludwig, A. Accelerated atomic-scale exploration of phase evolution in compositionally complex materials. *Materials Horizons* **5**, 86-92, doi:10.1039/C7MH00486A (2018).
- 23 Li, L., Kamachali, R. D., Li, Z. & Zhang, Z. Grain boundary energy effect on grain boundary segregation in an equiatomic high-entropy alloy. *Physical Review Materials* **4**, 053603, doi:10.1103/PhysRevMaterials.4.053603 (2020).
- 24 Wynblatt, P. & Chatain, D. Modeling grain boundary and surface segregation in multicomponent high-entropy alloys. *Physical Review Materials* **3**, 054004, doi:10.1103/PhysRevMaterials.3.054004 (2019).
- 25 Tang, M., Carter, W. C. & Cannon, R. M. Grain Boundary Transitions in Binary Alloys. *Physical Review Letters* **97**, 075502, doi:10.1103/PhysRevLett.97.075502 (2006).
- 26 Hart, E. W. 2-DIMENSIONAL PHASE TRANSFORMATION IN GRAIN BOUNDARIES. *Scripta Metall.* **2**, 179-&, doi:10.1016/0036-9748(68)90222-6 (1968).
- 27 Hu, C., Zuo, Y., Chen, C., Ping Ong, S. & Luo, J. Genetic algorithm-guided deep learning of grain boundary diagrams: Addressing the challenge of five degrees of freedom. *Materials Today*, doi:https://doi.org/10.1016/j.mattod.2020.03.004 (2020).
- 28 Zhou, N., Hu, T. & Luo, J. Grain boundary complexions in multicomponent alloys: Challenges and opportunities. *Current Opinion in Solid State and Materials Science* **20**, 268-277, doi:https://doi.org/10.1016/j.cossms.2016.05.001 (2016).
- 29 Morawiec, A. & Glowinski, K. On “macroscopic” characterization of mixed grain boundaries. *Acta Materialia* **61**, 5756-5767, doi:https://doi.org/10.1016/j.actamat.2013.06.019 (2013).
- 30 Li, L. *et al.* Segregation-driven grain boundary spinodal decomposition as a pathway for phase nucleation in a high-entropy alloy. *Acta Materialia* **178**, 1-9, doi:https://doi.org/10.1016/j.actamat.2019.07.052 (2019).
- 31 Larsen, P. M., Schmidt, S. & Schiøtz, J. Robust structural identification via polyhedral template matching. *Modelling and Simulation in Materials Science and Engineering* **24**, 055007, doi:10.1088/0965-0393/24/5/055007 (2016).
- 32 Luo, J. & Shi, X. M. Grain boundary disordering in binary alloys. *Appl. Phys. Lett.* **92**, 101901 doi:10.1063/1.2892631 (2008).
- 33 Luo, J. Developing Interfacial Phase Diagrams for Applications in Activated Sintering and Beyond: Current Status and Future Directions. *J. Am. Ceram. Soc.* **95**, 2358-2371, doi:10.1111/j.1551-2916.2011.05059.x (2012).
- 34 Wynblatt, P. & Ku, R. C. Surface energy and solute strain energy effects in surface segregation. *Surface Science* **65**, 511-531, doi:https://doi.org/10.1016/0039-6028(77)90462-9 (1977).
- 35 Xing, W., Kalidindi, A. R., Amram, D. & Schuh, C. A. Solute interaction effects on grain boundary segregation in ternary alloys. *Acta Materialia* **161**, 285-294, doi:https://doi.org/10.1016/j.actamat.2018.09.005 (2018).
- 36 Ogawa, H. GBstudio: A Builder Software on Periodic Models of CSL Boundaries for Molecular Simulation. *MATERIALS TRANSACTIONS* **47**, 2706-2710, doi:10.2320/matertrans.47.2706 (2006).
- 37 Plimpton, S. Fast Parallel Algorithms for Short-Range Molecular Dynamics. *Journal of Computational Physics* **117**, 1-19, doi:https://doi.org/10.1006/jcph.1995.1039 (1995).
- 38 Choi, W.-M., Jo, Y. H., Sohn, S. S., Lee, S. & Lee, B.-J. Understanding the physical metallurgy of the CoCrFeMnNi high-entropy alloy: an atomistic simulation study. *npj Computational Materials* **4**, 1, doi:10.1038/s41524-017-0060-9 (2018).
- 39 Hafner, G. K. a. J. Ab initio molecular dynamics for liquid metals. *Phys. Rev. B* **47**, 558 (1993).
- 40 G. Kresse, J. F. Efficient iterative schemes for ab initio total-energy calculations using a plane-wave basis set. *Phys. Rev. B* **54**, 11169 (1996).

- 41 Blochl, P. E. Projector augmented-wave method. *Phys. Rev. B* **50**, 17953 (1994).
42 G. Kresse, D. J. From ultrasoft pseudopotentials to the projector augmented-wave method *Phys.*
Rev. B **59**, 1758 (1999).
43 Leong, Z. *et al.* The Effect of Electronic Structure on the Phases Present in High Entropy Alloys.
Scientific Reports **7**, 39803, doi:10.1038/srep39803 (2017).
44 Manz, T. A. Introducing DDEC6 atomic population analysis: part 3. Comprehensive method to
compute bond orders. *RSC Advances* **7**, 45552-45581, doi:10.1039/C7RA07400J (2017).
45 Murdoch, H. A. & Schuh, C. A. Estimation of grain boundary segregation enthalpy and its role in
stable nanocrystalline alloy design. *Journal of Materials Research* **28**, 2154-2163,
doi:10.1557/jmr.2013.211 (2013).